J Therm Spray Tech (2021) 30:2187–2196
https://doi.org/10.1007/s11666-021-01270-3

PEER REVIEWED

Microstructure and Wear Resistance of Laser Clad $CoCrFeNiTiNbB_x$ High Entropy Alloy Coatings

Lin Ding[1] · Hongxin Wang[1]

Submitted: 27 March 2021 / in revised form: 9 October 2021 / Accepted: 13 October 2021 / Published online: 9 December 2021
© ASM International 2021

Abstract $CoCrFeNiTiNbB_x$ high entropy alloy coatings were prepared on AISI H13 steel using laser cladding. The effect of the boron content on the microstructure and wear resistance of the coatings was systematically investigated. Results showed that a TiB phase was formed in situ after adding boron, which promoted the formation of short rod-like dendrites and equiaxed crystals in the coatings underlying brittle fractures of massive coarse dendrites. The formation of macrocracks was not observed in the coatings after adding boron. The microstructure was more fine and uniform as the boron content increased. The microhardness and wear resistance of the coatings were gradually increased with the increase in the boron content. The microhardness and mass loss of the coatings were 1.25 and 0.61 times that of the coatings without boron, respectively, for a boron content of 1.25. The wear mechanism of the coatings was the adhesive wear and abrasive wear when the boron content was less than 1.0, and the abrasive wear when the boron content was not less than 1.0.

Keywords coatings · high entropy alloy · laser cladding · TiB · wear resistance

✉ Hongxin Wang
Wanghongxin7605@sohu.com

Lin Ding
dinglin8209@sohu.com

[1] School of Mechanical and Automotive Engineering, West Anhui University, Anhui 237012, China

Introduction

Die steel is widely employed in industry because it possesses high strength, toughness and excellent thermal fatigue stability. However, limited wear resistance of the die steel limits its application at room temperature and high temperature. In order to overcome this problem, feasible surface engineering techniques fabricating hard coatings are used to improve the wear properties on the surface of the die steel (Ref 1-4).

High entropy alloy (HEA) is an alloy containing five or more elements whose concentrations are between 5 and 35 at.%. Some research results revealed that high configurational entropy promotes the formation of a simple solid solution, while the intermetallic compound phases are not formed in the HEA and simultaneously makes HEA possess high hardness and good wear resistance (Ref 5-7). So far, HEA is mainly fabricated using arc melting (Ref 8), casting (Ref 9) and additive manufacturing (Ref 10, 11). However, the formation of the segregation and cavities, low efficiency and high cost limit the application of these methods. To solve these problems, some researchers have reported the HEA coatings prepared via surface engineering technologies, such as the magnetron sputtering (Ref 12), electrochemical deposition (Ref 13), plasma spray (Ref 14) and laser cladding (Ref 15). However, thin coatings produced using the former three methods reduce the performance advantage of the HEA. In addition, compared with the former three methods, laser cladding has the advantages of high heating and cooling rate, narrow heat-affected zone and excellent metallurgical bonding between the coatings and substrate.

High configurational entropy of B and some elements (Ti, Co, Cr, etc.) promotes the formation of borides increasing the strength and hardness of the HEA (Ref 16).

Furthermore, small atomic radius B is prone to occur the diffusion to form the fine crystal strengthening and solid solution strengthening effect, which improves the mechanical performance of the HEA (Ref 17). However, few papers involved $CoCrFeNiTiNbB_x$ HEA coatings prepared using laser cladding have been reported. Therefore, this paper aimed to research the effect of B content on the microstructure and wear resistance of the $CoCrFeNiTiNbB_x$ HEA coatings prepared using laser cladding, and the wear mechanism was also investigated.

Materials and Method

The substrate used in this study was H13 steel, whose chemical composition is listed in Table 1. The $CoCrFeNiTiNbB_x$ (x = 0.0, 0.5, 0.75, 1.0, 1.25) HEA cladding materials consisted of Co, Cr, Fe, Ni, Ti, Nb and B high purity (> 99.5%) powders mixed in nitrogen for 2 h using a planetary ball mill. The size of the powders was in a range of 50-100 μm. Before laser cladding, H13 steel surface was treated by grinding machine and cleaned by hydrous ethanol to remove dirt and oil. All the HEA powders and H13 steel were dried in an oven at 120 °C for 3 h. Then, the HEA powders were preset on H13 steel using the solution of sodium silicate. The thickness of the pre-coatings was approximately 1.2 mm.

$CoCrFeNiTiNbB_x$ high entropy alloy coatings were prepared using a 5 kW TJ-HL-T5000 CO_2 laser (λ = 10.64 μm). The processing parameters were as follows: a beam diameter of 5.0 mm, a scanning speed of 4 mm/s, a laser power of 2.5 kW, and an overlapping rate of 50%. A shielding of Ar gas was used to shield the molten pool.

The metallographic samples were cut, ground and polished in accordance with standard metallographic procedures and etched in the aqua regia for 120 s. The microstructure of the HEA coatings was observed using optical microscopy (OM; Olympus Pmc-3) and scanning electron microscope (SEM; Philip-Xl 30) system equipped with energy dispersive spectroscope (EDS) and transmission electron microscopy (TEM; H800). The phases of the HEA coatings were analyzed by x-ray diffraction (XRD; XD-3A) using 40 kV, 30 mA and Cu-Kα radiation and a scan speed of 1.23 °/min.

The microhardness of the HEA coatings was measured using an HV-1000 Vickers microhardness tester. The load applied was 4.9 N, the dwell time was 20 s, while the interval measured was 0.1 mm. The sliding-wear tests were conducted using a MM-200 block-on-wheel tribometer at room temperature. The cooling liquid was the emulsifier solution (1:100). Before testing, the surfaces of all HEA coatings samples with a size of 30 mm × 6.5 mm × 6.5 mm were ground and polished. The rotating counter wheel coated WC/Ni-based coatings (HRC 65) were used as the counterface material. The test load was 29.4 N, the rotational speed was 200 rpm, while the loading time was 60 min. Every sample was weighed every 10 min during the test. The worn surface of every sample was cleaned via anhydrous ethanol and then measured using an analytical balance with an accuracy of 0.0001 g. The morphologies of the worn samples were surveyed by SEM. The microhardness and mass loss of every sample were measured at least three times and then averaged.

Results and Discussion

Macro-morphology

Figure 1 shows the surface morphologies of the $CoCrFeNiTiNbB_x$ (x = 0.0 and 1.0) HEA coatings. As Fig. 1(a) demonstrates, several small-sized pores and cracks can be observed on the surface of the $CoCrFeNiTiNbB_{0.0}$ HEA coatings. No visible pores and cracks are observed on the surface of the $CoCrFeNiTiNbB_{1.0}$ HEA coatings, and the surface is more flat and smooth showing the superior qualities, Fig. 1(b). The shape parameters of the two HEA coatings evaluated are listed in Table 2. As Table 2 demonstrates, the $CoCrFeNiTiNbB_{1.0}$ HEA coatings have increased molten height, width and dilution ratio and a smaller wetting angle in comparison to the $CoCrFeNiTiNbB_{0.0}$ HEA coatings.

The reason of B improving the macro-forming quality of the HEA coatings, with there being several reasons for this. During the laser cladding process, B can form low melting point borates with oxygen mixed and oxides originating from the substrate due to its deoxidation, self-melting and slagging effects. These borates can cover the surface of the molten pool protecting it from excessive oxidation of the molten pool. The wettability of the liquid metal on the substrate is consequently improved, reducing the quantities of the inclusions and pores, leading to the improvement in

Table 1 Chemical composition of H13 steel (wt.%)

Element	C	Si	Mn	Cr	Mo	V	S	P
Content	0.32 ~ 0.45	0.80 ~ 1.20	0.2 ~ 0.5	4.75 ~ 5.50	1.10 ~ 1.75	0.80 ~ 1.20	≤ 0.03	≤ 0.03

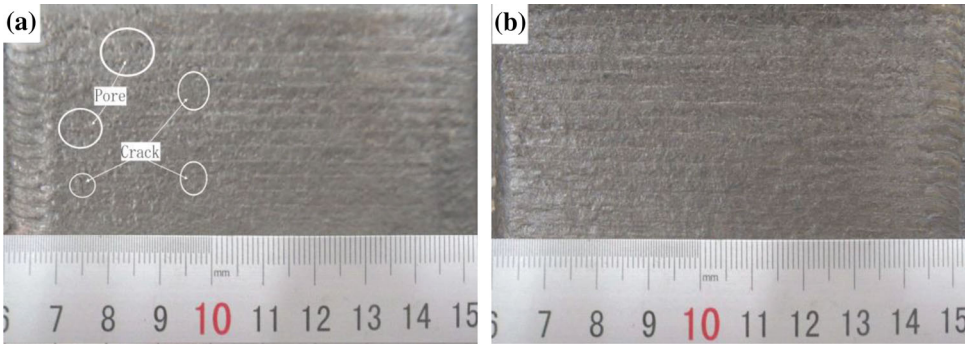

Fig. 1 Surface macro-morphologies of the $CoCrFeNiTiNbB_x$ HEA coatings (a) $x = 0.0$ (b) $x = 1.0$.

Table 2 Measurement and calculation results of shape parameters of the HEA coatings evaluated

Parameter	Thickness, mm	Molten height of the substrate, mm	Width, mm	Wetting angle, °	Dilution ratio, %
Measured result					
$x = 0.0$	1.01	0.10	4.54	52.6	9.01
$x = 1.0$	1.00	0.11	4.61	51.7	9.91

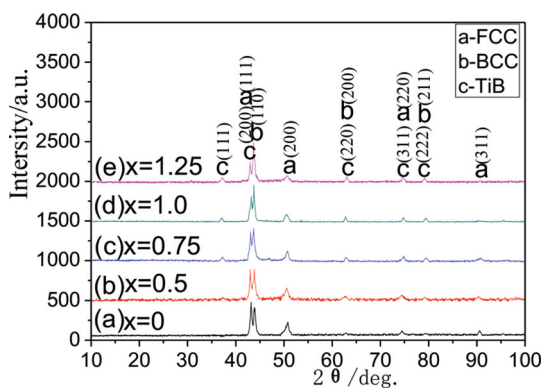

Fig. 2 XRD patterns of the $CoCrFeNiTiNbB_x$ HEA coatings (a) $x = 0.0$ (b) $x = 0.5$ (c) $x = 0.75$ (d) $x = 1.0$ (e) $x = 1.25$.

process formability of generating coatings on the substrate (Ref 18).

Phase Structures

Figure 2 shows the XRD patterns of the $CoCrFeNiTiNbB_x$ HEA coatings. $CoCrFeNiTiNbB_{0.0}$ HEA coatings consist primarily of face-centered cubic (FCC) and body-centered cubic (BCC) phases, Fig. 2(a). According to Gibbs phase law, if the alloy system is composed of n elements, the number of its equilibrium phases is $n + 1$. Only FCC and BCC phases are detected in the $CoCrFeNiTiNbB_{0.0}$ HEA coatings, far less than 7 phases calculated via the Gibbs phase law. This result is ascribed to the high entropy effect of the HEA. Based on Boltzmann hypothesis, the mixing entropy of a six-component HEA with an equal molar ratio is 1.792 *R*. (*R* is the gas constant.) The result indicates the formation of stable solid solution phases in the HEA coatings. Therefore, $CoCrFeNiTiNbB_{0.0}$ HEA coatings consist of only simple FCC and BCC phases (Ref 19).

Table 3 Mixing enthalpy (KJ/mol) of the constituent elements in the HEA

Element	Fe	Co	Cr	Ni	Ti	Nb	B
Fe	0	…	…	…	…	…	…
Co	− 1	0	…	…	…	…	…
Cr	− 1	− 4	0	…	…	…	…
Ni	− 2	0	− 7	0	…	…	…
Ti	31	18	31	13	0	…	…
Nb	− 16	− 25	− 7	− 30	2	0	…
B	− 26	− 24	− 31	− 24	− 58	− 54	0

Besides aforementioned constituent phases, a TiB phase is identified in the $CoCrFeNiTiNbB_x$ HEA coatings after adding B, Fig. 2(b), (c), (d), and (e). According to Gibbs free energy law, whether the phase transition can occur is dependent on changes of the enthalpy, as well as the entropy. The mixing enthalpy of the reaction between constituent elements is an important parameter to evaluate whether the chemical reaction can continue spontaneously. The mixing enthalpy of the constituent elements in the HEA is presented in Table 3 (Ref 20). The more negative the mixing enthalpy of the constituent elements is, the easier progress the reaction of the constituent elements will. As Table 3 demonstrates, the mixing enthalpy of the boride formed by B and Ti elements has the most negative, which offsets partial inter-solubility of the constituent elements in the HEA and simultaneously promotes

additional nucleation and growth of TiB. However, the high entropy effect restrains the formation of other intermetallic compounds in the coatings. Previously published literature (Ref 21) indicates that the reaction product of B and Ti is TiB_2. However, TiB_2 phase is not detected in this work. A potential reason for this is that B and Ti initially form TiB_2 during the laser cladding process, following which TiB_2 formed and excess Ti react to form TiB due to the instability of TiB_2 (Ref 22).

In addition, the intensities of the FCC phase diffraction peak are gradually decreased as B content increases, while the intensities of the TiB and BCC phases diffraction peaks are gradually increased, illustrating the improvement of BCC and TiB phases in content and the reduction of the FCC phase in content in the HEA coatings, Fig. 2(b), (c), (d), and (e). The primary reason for this result is that the solid solubility of B in the FCC lattice is gradually increased as B content increases. The lattice distortion of the FCC phase is increased, and the diffuse reflection effect is enhanced, resulting in the reduction of the diffraction peak intensities of the FCC phase (Ref 23). In addition, B is helpful to the formation of BCC phase. The addition of B adjusts the strain of the BCC phase lattice, reducing the systematic free energy, and stabilizing the phase structure. The increase in B content is directly correlated with the formation of TiB.

Microstructure

Figure 3 shows the microstructure of the $CoCrFeNiTiNbB_x$ HEA coatings. As Fig. 3(a) and (b) demonstrates, the microstructure of the $CoCrFeNiTiNbB_{0.0}$ HEA coatings typically consists of three phases: white bright planar bonding zone located at the bonding interface, cellular dendrites and coarse dendrites located in the lower region, and some short rod-like dendrites and equiaxed crystal in the upper region. The formation of these phases is ascribed to the differences in temperature gradient and the instantaneous solidification velocity of different positions in the molten pool. The appearance of the white bright planar bonding zone further provides evidence for the formation of excellent metallurgical bonding between the coatings and substrate (Ref 24).

The microstructure of the $CoCrFeNiTiNbB_x$ HEA coatings is not obviously changed after adding B. However, more short rod-like dendrites and equiaxed crystals appear in the HEA coatings. The quantity of these short rod-like dendrites and equiaxed crystals is gradually increased as B content increases. The microstructure is more fine and uniform, Fig. 3(c), (d), (e), (f), (g), (h), and (j). Adding B has two effects. Firstly, small B atoms are easily solid-soluted in the dendrites during the laser cladding process, which form the supersaturated solid solution increasing the lattice distortion and lattice strain energy. These supersaturated B atoms will precipitate and diffuse to the interfacial frontier of the liquid–solid during the subsequent solidification process, which reduce the strain energy and increase the undercooling of the liquid metal. Therefore, fine and short rod-like dendrites and equiaxed crystals are formed in the HEA coatings. Secondly, TiB formed will increase the quantity of heterogeneous nucleation cores in the liquid metal, hindering the formation of coarse dendrites. The microstructure of the HEA coatings is further refined.

Figure 4 shows SEM morphologies of the $CoCrFeNiTiNbB_{1.0}$ HEA coatings. Some polygonal shaped phases are observed to precipitate in the HEA coatings, Fig. 4. The EDS analysis results of the correspondingly marked zones in Fig. 4(b) are presented in Table 4. As Table 4 demonstrates, the dendrite (Zone A) primarily consists of large concentrations of Fe, Ni and Co elements, while the interdendritic eutectic (Zone B) has significant quantities of Fe, Cr and Nb. Fe content in the dendrites and interdendritic region is in excess to the element ratio of the HEA coatings materials owing to the dilution effect of the substrate. The polygon-shaped precipitation (Zone C and D) consists of Ti and B elements. B atoms dissolved in the dendrites from the lattice distortion improving the instability of the lattice. Therefore, B atoms are preferentially located in the interdendritic region. As reported in Table 3, Nb, Ti and Cr atoms are enriched in the interdendritic region due to the highly negative hybrid enthalpy of Nb-B, Ti-B and Cr-B. However, Nb and Cr atoms are mainly solid-soluted into the interdendritic region owing to the largest negative mixing enthalpy of Ti-B. The precipitation of the TiB phase indicates that B atoms in the solid solution are not replaced by other atoms and will form new phases with other atoms. This result is ascribed to selective solidification and crystallization of the HEA. B and Ti atoms will be continuously incorporated into the interdendritic region during the solidification process. A great number of TiB nucleation cores are formed as the ratio of B and Ti atoms reaches a critical value of TiB formed, following which they gradually precipitate during the last solidification process (Ref 25). In light of the analysis results of XRD and EDS data, the dendrite (Zone A) is a BCC phase, the interdendritic eutectic (Zone B) is a FCC phase, and the polygon precipitation (Zone C and D) is a TiB phase.

TEM images of the microstructure showing the equiaxed crystal zone in Fig. 3(g) and (h) are exhibited in Fig. 5. The images demonstrate a gray coarse crystal of the $CoCrFeNiTiNbB_{0.0}$ HEA coatings, which is in agreement with the microstructure observed, Fig. 5(a). However, $CoCrFeNiTiNbB_{1.0}$ HEA coatings exist fine gray crystal and gray white polygonal phase, Fig. 5(b). The selected area electron diffraction (SAED) patterns and EDS results

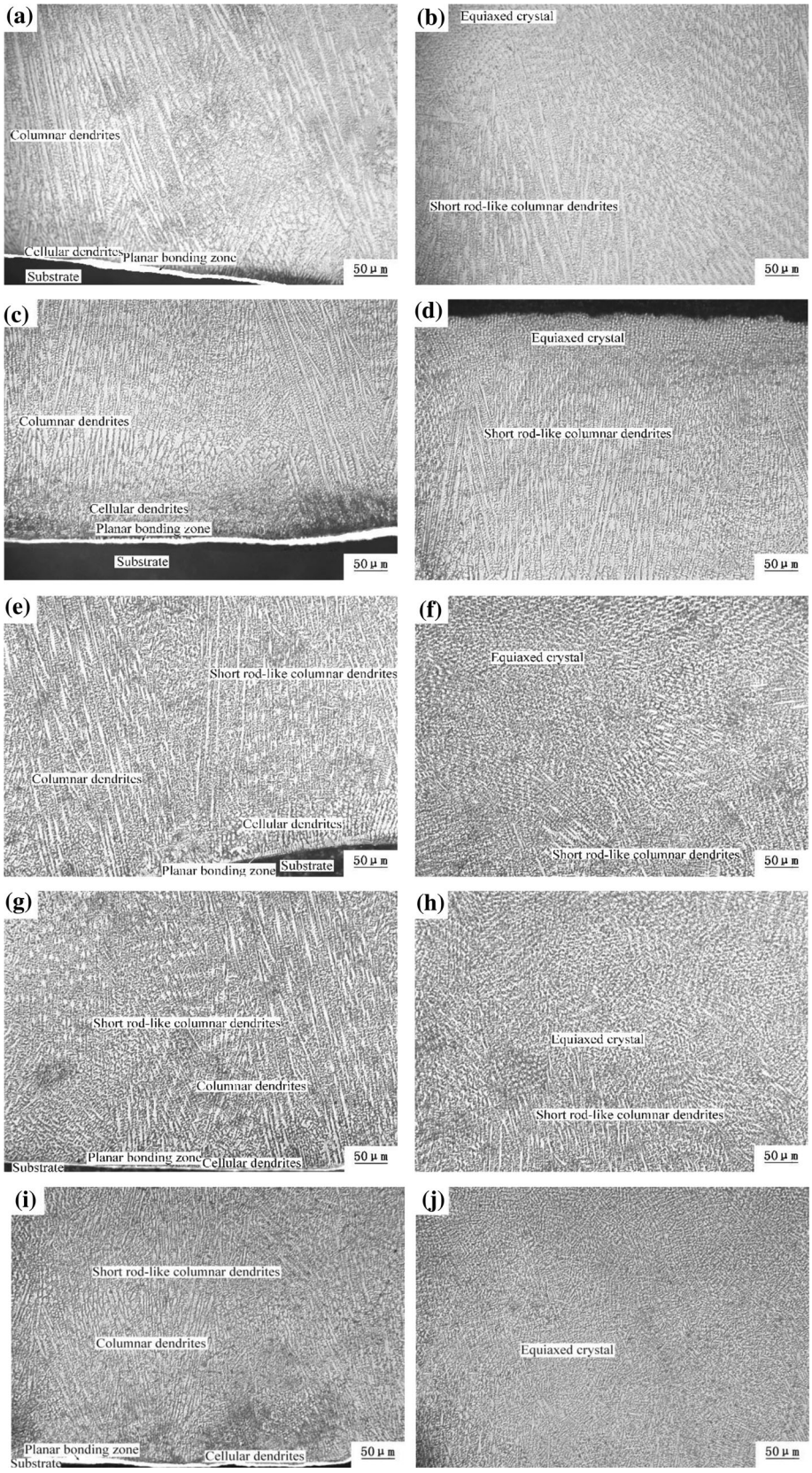

Fig. 3 Microstructure of the $CoCrFeNiTiNbB_x$ HEA coatings (a) and (b) $x = 0.0$ (c) and (d) $x = 0.5$ (e) and (f) $x = 0.75$ (g) and (h) $x = 1.0$ (i) and (j) $x = 1.25$.

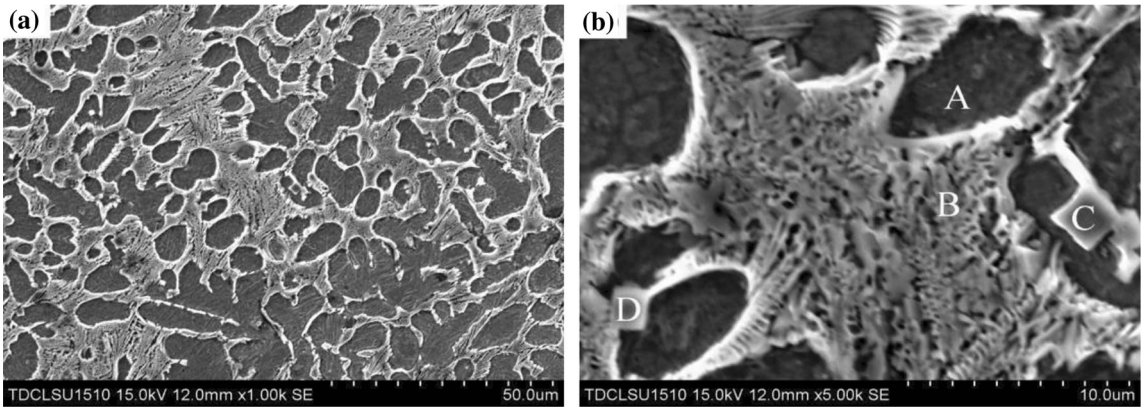

Fig. 4 SEM morphologies of the $CoCrFeNiTiNbB_{1.0}$ HEA coatings (a) Morphologies at a low magnification (b) Morphologies at a high magnification.

Table 4 EDS results of the marked zones in Fig. 4 (wt.%)

Zone	Element						
	Fe	Co	Cr	Ni	Ti	Nb	B
A	36.67	18.73	8.85	20.23	6.11	6.65	2.76
B	35.46	6.52	18.34	7.75	4.17	24.89	2.87
C	0.56	…	0.27	…	59.65	1.23	38.28
D	1.04	0.18	0.62	…	63.24	1.52	33.39

of the TiB phase (zone A), exhibited in Fig. 5(b) and (c), clearly infer the existence of an in situ TiB phase with a cubic structure along the $[02\bar{2}]$ zone axis, which is supported by the XRD results. The formation of TiB formed produces the strong pinning effect on the grain boundary, further restricting grain growth, leading to the refinement of the microstructure in the $CoCrFeNiTiNbB_{1.0}$ HEA coatings (Ref 26).

In order to further understand the formation of TiB phase in the $CoCrFeNiTiNbB_x$ HEA coatings, and the schematic illustration of the solidification process of the $CoCrFeNiTiNbB_x$ HEA system during the laser cladding process is shown in Fig. 6. Firstly, the powder particles of the $CoCrFeNiTiNbB_x$ system are gradually melted by the laser beam and form the molten pool, Fig. 6(a) and (b). Secondly, decomposed Ti and B atoms form TiB_2 in the molten pool due to the lowest mixing enthalpy of the Ti-B and high entropy effect of the HEA. During the subsequent solidification process, TiB_2 nucleates and precipitates from the molten pool ($L \rightarrow TiB_2$), and following which it slowly grows due to the lower B content of HEA powders, Fig. 6(c). Thirdly, TiB_2 generated and react with Ti of the surrounding liquid metal to form TiB ($L + TiB_2 \rightarrow TiB$), as the ratio of Ti and TiB_2 reaches to the condition that facilitates the peritectic transformation, Fig. 6(d). Finally, during the continued development of the solidification process, in situ TiB particles will gradually increase in size due to the component and energy fluctuation of the molten pool. To facilitate the diagram, the formation of BCC and FCC phases is not shown in Fig. 6. Based on previous analysis, it is well known that the addition of B promotes the formation of a TiB phase, refining the microstructure, resulting in the enhanced performance of the HEA coatings.

Microhardness

Figure 7 shows the microhardness distribution of the $CoCrFeNiTiNbB_x$ HEA coatings. As Fig. 7 demonstrates, the average microhardness value of the substrate is 285.09 HV. The average microhardness value of the $CoCrFeNiTiNbB_{0.0}$ HEA coatings is 481.57 HV, approximately 1.7 times that of the substrate. The average microhardness value of the $CoCrFeNiTiNbB_x$ ($x = 0.5$, 0.75, 1.0) HEA coatings is 522.73 HV, 557.63 HV and 589.42 HV, respectively, which is an improvement of 8.55, 15.79 and 22.40%. The main reason is that high entropy effect of the HEA and fast solidification of laser cladding promotes alloy elements dissolve into the HEA matrix and form the solid solution strengthening effect. However, the size of the microstructure in the $CoCrFeNiTiNbB_{0.0}$ HEA coatings is larger, and consequently, the microhardness is reduced. A few TiB formed disperse in the $CoCrFeNiTiNbB_x$ HEA coatings after adding B, which has a dispersion strengthening effect, leading to the improvement in microhardness of the HEA coatings.

In addition, the precipitation of TiB formed along the grain boundary causes grain boundary panning, hindering the grain boundary migration, leading to the improvement in microhardness of the HEA coatings. According to the Orowan mechanism of the dislocation theory, when the glide dislocation of Burgers vectors b bypasses the hard particles with a space λ, the external stress τ is calculated as:

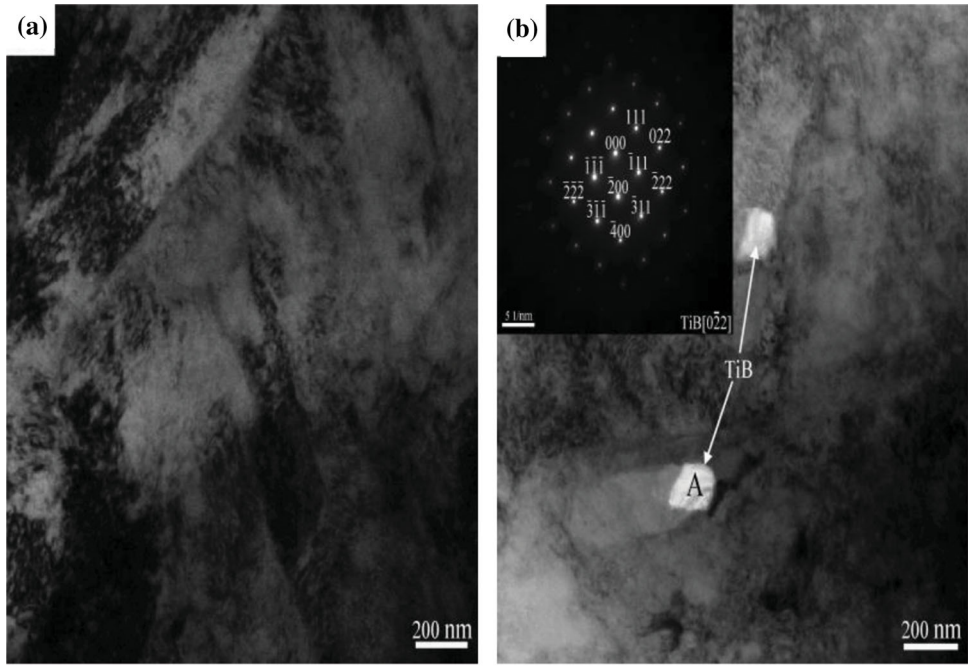

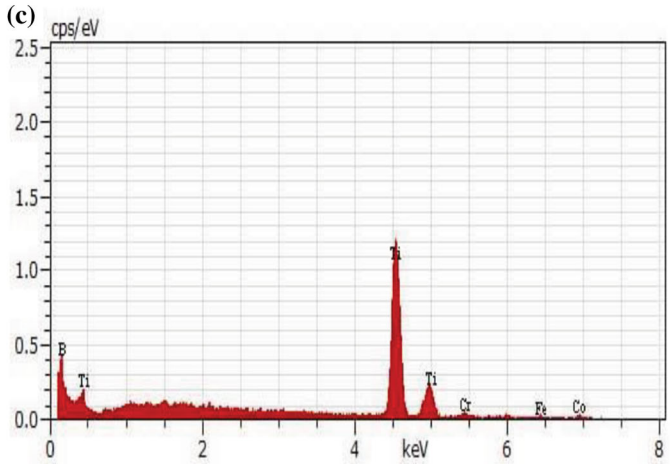

Fig. 5 TEM images of the microstructure showing the equiaxed crystal zone in Fig. 3 (g) and (h) (a) TEM images of the $CoCrFeNiTiNbB_{0.0}$ (b) TEM images of the $CoCrFeNiTiNbB_{1.0}$ and SAED patterns of TiB phase (c) EDS result of region A in (b).

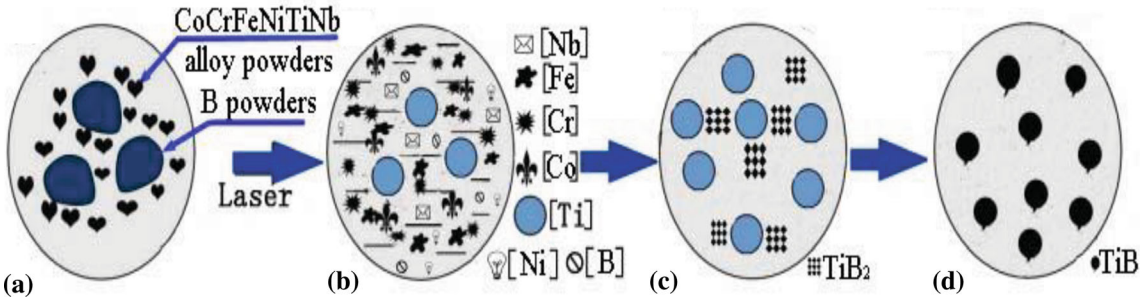

Fig. 6 Schematic illustration of the solidification process of the $CoCrFeNiTiNbB_x$ HEA coatings during the laser cladding process.

$$\tau = Gb/\lambda$$

where G is the elastic modulus. The amount of TiB formed in the $CoCrFeNiTiNbB_{0.0}$ HEA coatings is gradually increased as B content increases, and the space λ of the TiB particles is gradually decreased. The smaller the space (λ) of the TiB particles is, the larger the external stress (τ) and the resistance of the glide dislocation are. The microhardness of the HEA coatings is gradually improved as B

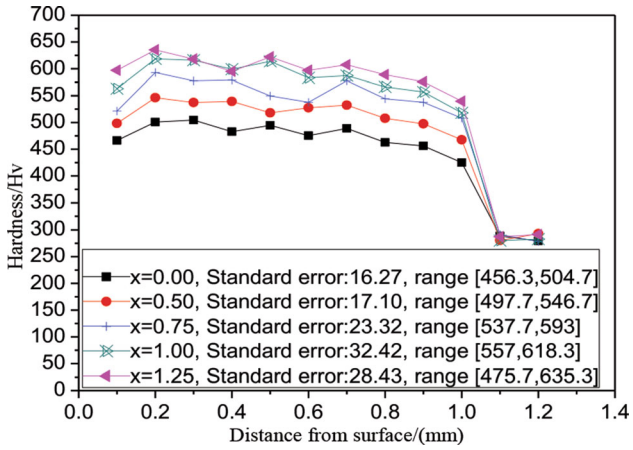

Fig. 7 Microhardness distribution of the $CoCrFeNiTiNbB_x$ HEA coatings.

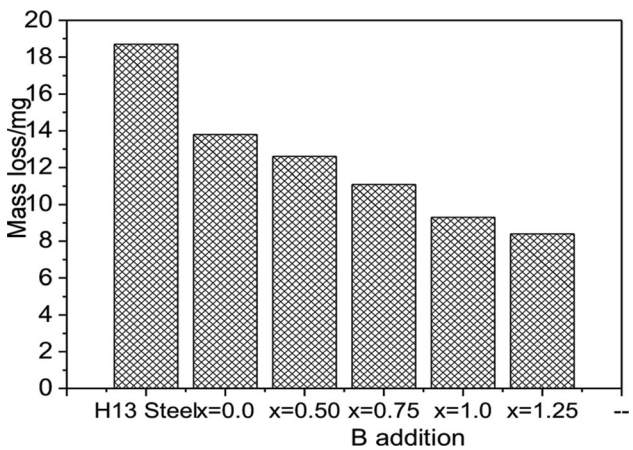

Fig. 8 Mass loss of the substrate and $CoCrFeNiTiNbB_x$ HEA coatings.

content increases. In addition, B element promotes the formation of the BCC phase, which further improves the microhardness of the HEA coatings.

The average microhardness of the $CoCrFeNiTiNbB_{1.25}$ HEA coatings is 604.13 HV, approximately 2.1 times that of the substrate, Fig. 7. Compared with $CoCrFeNiTiNbB_{0.0}$ HEA coatings, the average microhardness of the $CoCrFeNiTiNbB_{1.25}$ HEA coatings is improved by 25.45%. However, the extent of improvement in microhardness of the HEA coatings is decreased. This is likely due to excess B dissolves into the HEA matrix forming the supersaturated solid solution owing to the limited Ti content. Therefore, the microhardness of the $CoCrFeNiTiNbB_{1.25}$ HEA coatings is slightly increased.

Wear Resistance

Figure 8 shows the mass loss of the substrate and $CoCrFeNiTiNbB_x$ HEA coatings. As Fig. 8 demonstrates, the mass loss of the $CoCrFeNiTiNbB_{0.0}$ HEA coatings is 13.8 mg, approximately 3/4 of the substrate. The mass loss of the $CoCrFeNiTiNbB_x$ (0.5, 0.75, 1.0) HEA coatings is 12.6 mg, 11.1 mg and 9.3 mg, respectively. Compared with the $CoCrFeNiTiNbB_{0.0}$ HEA coatings, the mass loss of the $CoCrFeNiTiNbB_x$ (0.5, 0.75, 1.0) HEA coatings is decreased by 8.70%, 19.57% and 32.61%, respectively. This result is mainly ascribed to the dispersion strengthening effect and fine crystal strengthening effect of hard TiB dispersed in the HEA coatings. The quantity of hard TiB formed by the reaction is gradually increased as B content increases. The mass loss of the $CoCrFeNiTiNbB_{1.25}$ HEA coatings is 8.4 mg, which is, respectively, 60.87% and 44.92% that of the $CoCrFeNiTiNbB_{0.0}$ HEA coatings and substrate (Fig. 8). The results are explained by the solid solution strengthening effect of excess B dissolved into the HEA matrix, leading to further reduction in mass loss of the HEA coatings. In a word, the higher the microhardness of the HEA coatings, the smaller the mass loss is (Ref 27).

Figure 9 shows the worn surface morphologies of the substrate and $CoCrFeNiTiNbB_x$ HEA coatings. As Fig. 9(a) demonstrates, the worn surface of the substrate exhibits a large number of wide and deep furrows, serious plastic deformation, exfoliation and adhesion features. The reason is to be expected as the microhardness of the substrate is low. Large amounts of debris exfoliated enter into the friction pair forming the three-body abrasion to aggravate the surface wear, resulting in the formation of wide and deep furrows on the worn surface. Partial of exfoliation covering the worn surface under the friction force forms the adhesion phenomenon. The wear mechanism of the substrate is typical characteristic of the abrasive wear and adhesive wear.

Compared with the substrate, the surface wear of the $CoCrFeNiTiNbB_{0.0}$ HEA coatings is obviously alleviated. However, the worn surface of the HEA coatings still appears to have some plastic deformation, wider and deeper furrows, debris exfoliation and accumulation and adhesion, Fig. 9(b). The wear mechanism of the $CoCrFeNiTiNbB_{0.0}$ HEA coatings is still the abrasive wear and adhesive wear. The reason is that the large quantity of alloy elements is dissolved into the HEA matrix causing the solid solution strengthening effect, resulting in the improvement in wear resistance of the HEA coatings.

The worn surface of the $CoCrFeNiTiNbB_x$ HEA coatings after adding B appears slight plastic deformation, a small number of shallow and narrow furrows, as well as debris accumulation, Fig. 9(c), (d), (e), and (f). These features are reduced in severity as B content increases, the worn surface is more smooth and uniform. The wear mechanism of the HEA coatings is the abrasive wear and

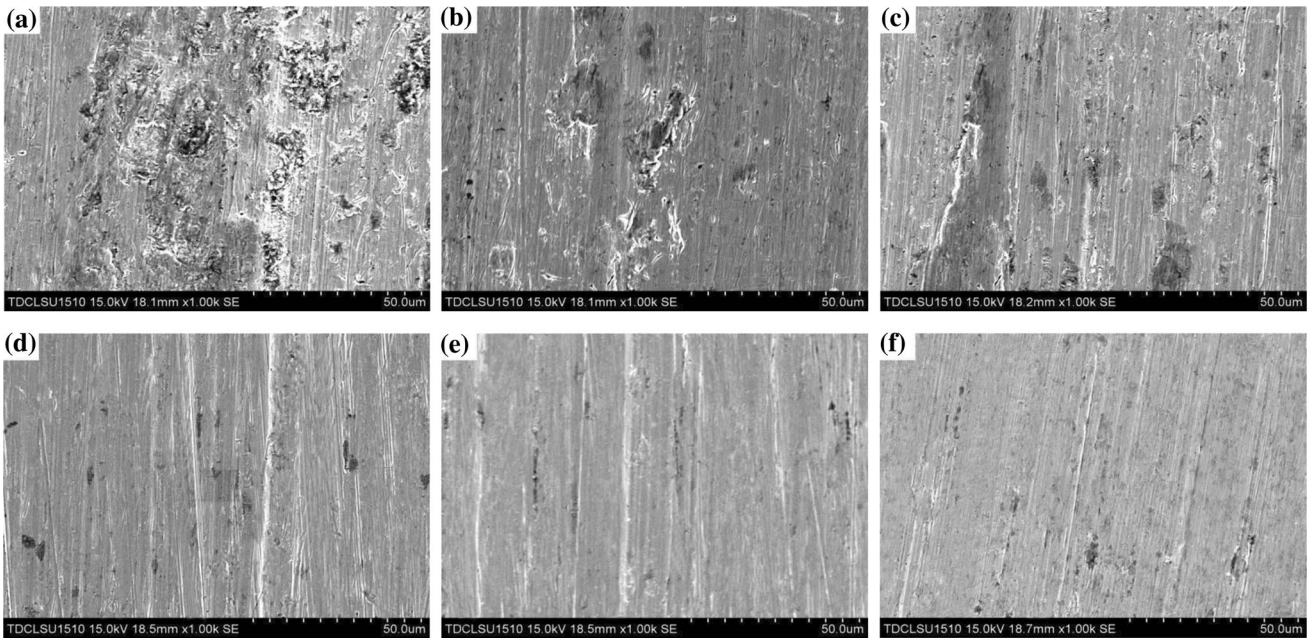

Fig. 9 Worn surface morphologies of the substrate and $CoCrFeNiTiNbB_x$ HEA coatings (a) substrate (b) $x = 0.0$ (c) $x = 0.5$ (d) $x = 0.75$ (e) $x = 1.0$ (f) $x = 1.25$.

adhesive wear when the B content is less than 1.0 and is the abrasive wear when the B content is not less than 1.0.

Adding B can effectively improve the wear resistance of the $CoCrFeNiTiNbB_x$ HEA coatings. The primary reason is that hard TiB dispersed in the HEA coatings has the dispersion strengthening and simultaneously forms a good bonding with the HEA matrix, which improves the wear resistance of the coatings. Lots of hard TiB particulates dispersing on the surface of the HEA coatings increase the friction resistance of the grinding ring during the friction process. The more B content is, the more TiB formed. In addition, some lattice distortion and stress exist between the HEA matrix and TiB formed by in situ reaction, which increases the resistance of the dislocation motion, leading to further improvement in wear resistance of the HEA coatings (Ref 28). Finally, more B atoms dissolved into the HEA matrix cause the solid solution strengthening effect as the B content increases, resulting in further improvement in wear resistance of the HEA coatings.

Conclusions

(1) In situ synthesized TiB phase was identified in the $CoCrFeNiTiNbB_x$ HEA coatings after adding B, besides mentioned FCC and BCC phases in the $CoCrFeNiTiNbB_{0.0}$ HEA coatings. The quantity of the TiB phase was gradually increased with the increase of B content.

(2) The microstructure of the $CoCrFeNiTiNbB_x$ HEA coatings consisted of a white bright planar bonding zone, coarse columnar dendrites and a few equiaxed crystals. More short rod-like dendrites and equiaxed crystals appeared in the HEA coatings as B content increased, and the microstructure was finer and more uniform.

(3) The average microhardness of the $CoCrFeNiTiNbB_x$ HEA coatings was gradually increased as B content increased, and the change in mass loss was opposite. The highest microhardness of the HEA coatings with a B content of 1.25 was 604.13 HV, approximately 1.25 and 2.1 times that of the $CoCrFeNiTiNbB_{0.0}$ HEA coatings and substrate, respectively. The lowest mass loss of the HEA coatings with a B content of 1.25 was 8.4 mg, approximately 0.61 and 0.45 times that of the $CoCrFeNiTiNbB_{0.0}$ HEA coatings and substrate, respectively. The wear mechanism of the $CoCrFeNiTiNbB_x$ HEA coatings was the abrasive wear and adhesive wear when the B content was less than 1.0 and was the abrasive wear when the B content was not less than 1.0.

Acknowledgments One of the authors, Lin Ding, gratefully acknowledges the financial support of Excellent Young Talents Fund Program of Higher Education Institutions of Anhui Province of China (No. gxyq2019073) and High Level Talents Support Project of West Anhui University (No. WGKQ201802005).

References

1. M.R. Fernández, A. García, J.M. Cuetos et al., Effect of Actual WC Content on the Reciprocating Wear of a Laser Cladding NiCrBSi Alloy Reinforced with WC, *Wear*, 2015, **324-325**, p 80-89.
2. D. Verdi, M.A. Garrido, C.J. Múnez et al., Microscale Effect of High-Temperature Exposition on Laser Cladded Inconel625-Cr_3C_2 Metal Matrix Composite, *J. Alloy. Compd.*, 2017, **695**, p 2696-2705.
3. Hu. Ding Lin, Q.X. Shengsun et al., Effect of Ti on the Microstructure Evolution and Wear Behavior of VNalloy/Co-Based Composite Coatings by Laser Cladding, *J. Mater. Process. Technol.*, 2018, **252**, p 711-719.
4. Q. Xiumin and D. Lin, Microstructure and Wear Resistance of Nano-Sm_2O_3 Reinforced TiC/Co-Based Composite Coatings, *Tribology*, 2020, **40**, p 49-59.
5. Y. Ma, Q. Wang, B.B. Jiang et al., Controlled Formation of Coherent Cuboidal Nanoprecipitates in Body-Centered Cubic High-Entropy Alloys Based on Al_2(Ni Co, Fe, C_r)14 Compositions, *Acta Mater.*, 2018, **147**, p 213-225.
6. J.B. Seol, J.W. Bae, Z.M. Li et al., Boron Doped Ultrastrong and Ductile High-Entropy Alloys, *Acta Mater.*, 2018, **151**, p 366-376.
7. N.D. Stepanov, D.G. Shaysultanov, R.S. Chernichenko et al., Effect of Thermomechanical Processing on Microstructure and Mechanical Properties of the Carbon-Containing CoCrFeNiMn High Entropy Alloy, *J. Alloys Compd.*, 2017, **693**, p 394-405.
8. H. Zhang Jian, W.Q. Yeyuan et al., Microstructure and Mechanical Properties of RexNbMoTaW Highentropy Alloys Prepared by Arc Melting Using Metal Powders, *J. Alloys Compd.*, 2020, **827**, p 1-8.
9. M.-G. Larissa, M. Igor, O. Milan et al., High-Strength Al0.2Co1.5CrFeNi1.5Ti High-Entropy Alloy Produced by Powder Metallurgy and Casting: A Comparison of Microstructures Mechanical and Tribological Properties, *Mater. Charact.*, 2020, **159**, p 1-16.
10. L. Danyang, X. Lianyong, J. Hongyang et al., A Strong, Ductile, High-Entropy FeCoCrNi Alloy with Fine Grains Fabricated Via Additive Manufacturing and a Single Cold Deformation and Annealing Cycle, *Addit. Manuf.*, 2020, **36**, p 101591.
11. L. Danyang, X. Lianyong, L. Xiaojie et al., A Si-Containing FeCoCrNi High-Entropy Alloy with High Strength and Ductility Synthesized In Situ Via Selective Laser Melting, *Addit. Manuf.*, 2020, **35**, p 101340.
12. W. Liao, S. Lan, L. Gao et al., Nanocrystalline High-Entropy Alloy (CoCrFeNiAl0.3) Thin-Film Coating by Magnetron Sputtering, *Thin Solid Films*, 2017, **638**, p 383-388.
13. V. Soare, M. Burada, I. Constantin et al., Electrochemical Deposition and Microstructural Characterization of AlCrFeMnNi and AlCrCuFeMnNi High Entropy Alloy Thin Films, *Appl. Surf. Sci.*, 2015, **358**, p 533-539.
14. M. Ashok, A. Ameey, L. Vladimir et al., Multiscale Mechanical Performance and Corrosion Behaviour of Plasma Sprayed AlCoCrFeNi High-Entropy Alloy Coatings, *J. Alloys Compd.*, 2020, **854**, p 157140.
15. F.Y. Shu, S. Liu, H.Y. Zhao et al., Structure and High-Temperature Property of Amorphous Composite Coating Synthesized by Laser Cladding FeCrCoNiSiB High-Entropy Alloy Powder, *J. Alloy. Compd.*, 2018, **731**, p 662-666.
16. Y. He, J. Zhang, H. Zhang et al., Effects of Different Levels of Boron on Microstructure and Hardness of CoCrFeNiAlxCu0.7-Si0.1By High-Entropy Alloy Coatings by Laser Cladding, *Coatings*, 2017, **7**(7), p 1-7.
17. L. Danyang, Z. Nannan, He. Bin et al., Tribological Properties of $FeCoCrNiAlB_x$ High-Entropy Alloys Coating Prepared by Laser Cladding, *J. Iron. Steel Res. Int.*, 2017, **24**, p 184-189.
18. H. Zufeng, Z. Chong, T. Qunhua et al., Effects of Annealing on the Microstructure and Hardness of Laser Cladding FeCoCrNiB High-Entropy Alloy Coating, *Surf. Technol.*, 2013, **42**(1), p 9-13.
19. Y. Wang, S. Ma, X. Chen et al., Optimizing Mechanical Properties of AlCoCrFeNiTix High-Entropy Alloys by Tailoring Microstructures, *Acta Metall. Sin.*, 2013, **26**(3), p 277-284.
20. A. Takeuchi and A. Inoue, Classification of Bulk Metallic Glasses by Atomic Size Difference, Heat of Mixing and Period of Constituent Elements and Its Application to Characterization of the Main Alloying Element, *Mater. Trans.*, 2005, **46**(12), p 2817-2829.
21. L. Han, M. Lingling, W. Chaoqun et al., Microstructure and Properties of Laser Cladding $AlB_xCoCrNiTi$ High-Entropy Alloy Coating on Titanium Alloys, *Surf. Technol.*, 2017, **46**(6), p 226-231.
22. L. Min, H. Jian, Z. Yan-Yan et al., Growth Morphology and Solidification Behavior of In-Situ Synthesized TiN and TiB, *Mater. Trans.*, 2016, **57**(1), p 15-19.
23. Q.S. Chen, Y. Lu, Y. Dong et al., Effect of Minor B Addition on Microstructure and Properties of AlCoCrFeNi Multi-component Alloy, *Trans. Nonferrous Met. Soc. China*, 2015, **25**(9), p 2958-2964.
24. R. Li, Z. Li, J. Huang et al., Dilution Effect on the Formation of Amorphous Phase in the Laser Cladded Ni-Fe-B-Si-Nb Coatings After Laser Remelting Process, *Appl. Surf. Sci.*, 2012, **258**, p 7956-7961.
25. Hu. Wang, W. Zhihui, Li. Hongbo et al., Microstructure Characterization of In-Situ Synthesized VC Reinforced CoCrCuFeNiMn High-entropy Alloy-Based Coatings by Plasma Cladding, *Surf. Technol.*, 2018, **47**(8), p 271-275.
26. J. Wang, H. Yang, Z. Liu et al., A Novel $Fe_{40}Mn_{40}Cr_{10}Co_{10}$/SiC Medium-Entropy Nanocomposite Reinforced by the Nanoparticles-Woven Architectural Structures, *J. Alloys Compd.*, 2019, **772**, p 272-279.
27. Li. Hengde and X. Jimei, *Surface and Interface in Materials*, Tsing hua University Press, Beijing, 1990.
28. Z. Weiping, L. Shuo and Ma. Yutao, Strengthening Mechanism of Particle Reinforced Metal Matrix Composite Coating by Laser Cladding, *Trans. Mater. Heat Treat.*, 2005, **26**(1), p 70-73.

Publisher's Note Springer Nature remains neutral with regard to jurisdictional claims in published maps and institutional affiliations.